High-contrast visible nulling coronagraph for segmented and arbitrary telescope apertures

Brian A. Hicks[*a], Richard G. Lyon[a], Matthew R. Bolcar[a], Mark Clampin[a], and Peter Petrone[b]

[a]NASA Goddard Space Flight Center, Greenbelt, MD, USA;
[b]Sigma Space Corporation, Lanham, MD, USA

ABSTRACT

Exoplanet coronagraphy will be driven by the telescope architectures available and thus the system designer must have available one or more suitable coronagraphic instrument choices that spans the set of telescope apertures, including filled (off-axis), obscured (e.g. with secondary mirror spiders and struts), segmented apertures, such as JWST, and interferometric apertures. In this work we present one such choice of coronagraph, known as the visible nulling coronagraph (VNC), that spans all four types of aperture and also employs differential sensing and control.

Keywords: Exoplanets, high contrast imaging, visible nulling coronagraph, segmented telescopes, wavefront sensing and control, nulling interferometry, polarization optics

1. INTRODUCTION

The direct detection and characterization of exoplanetary systems including exoplanets, dust, and debris disks, is a crucial step in the search for habitable planets with liquid water, and potentially life. The visible nulling coronagraph (VNC) is an approach to high-contrast imaging being developed to enable such observations at both the component and system level, having been proposed for both probe-class[1] and stratospheric balloon[2] missions. As an instrument, VNC has demonstrated 10^{-9} contrast averaged over an inner to outer working angle of $1 - 4\lambda/D$ in polarized narrowband (1.2 nm FWHM) light,[3] the level and separation required to detect and characterize dust, debris disks, and exo-Jupiters in nearby systems. At the system level, the VNC is a viable option for a variety of planned mission telescope architectures, including the obscured 2.4-m Wide-Field Infrared Survey Telescope (WFIRST) aperture,[4] and in the more distant future the Advanced Technology Large Aperture Space Telescope (ATLAST), which is currently favored to be a 10-m or greater segmented aperture.[5]

The VNC approach spans all future flight telescope architectures including filled (both on- and off-axis), segmented, and sparse aperture telescope systems. Additionally it makes use of all the available output photons for null control since the flux from the target star is conserved from the bright and dark output channels of the VNC. This conservation law yields a robust null control approach that is independent of the state of instrument and its control temporal bandwidth depends only on the brightness of the target star. It does not levy beyond state of the art stability requirements on the telescope since the telescope must be stable only over each integration window for null control.

The next milestone to be demonstrated with the VNC is 10^{-9} contrast at an increased spectral bandpass of 40 nm FWHM. This will be accomplished using achromatic phase shifters (APS) that equalize the optical phase difference to π within the 40 nm spectral bandpass for both polarization states simultaneously. Schemes studied for introducing a broadband, polarization independent π phase delay for nulling include transmission through dielectric plates[6] and Fresnel rhomb retarders.[7] These approaches have been revisited for use within the VNC.[8] Here we discuss tolerancing of Fresnel rhomb retarders based on practical limits to fabrication capabilities and compensation of these imperfections by positioning the rhombs' fine angular orientation using optoelectromechanical sensing and control. The key advantage of the VNC paired with Fresnel rhomb as an approach to broadband suppression is that, unlike theoretically achromatic techniques using field rotation,[9,10] there is no twin planet problem and reduced sensitivity to the finite angular extent of the stellar disk.

*brian.a.hicks@nasa.gov

Space Telescopes and Instrumentation 2014: Optical, Infrared, and Millimeter Wave, edited by Jacobus M. Oschmann, Jr., Mark Clampin, Giovanni G. Fazio, Howard A. MacEwen, Proc. of SPIE Vol. 9143, 91432S · © 2014 SPIE
CCC code: 0277-786X/14/$18 · doi: 10.1117/12.2056296

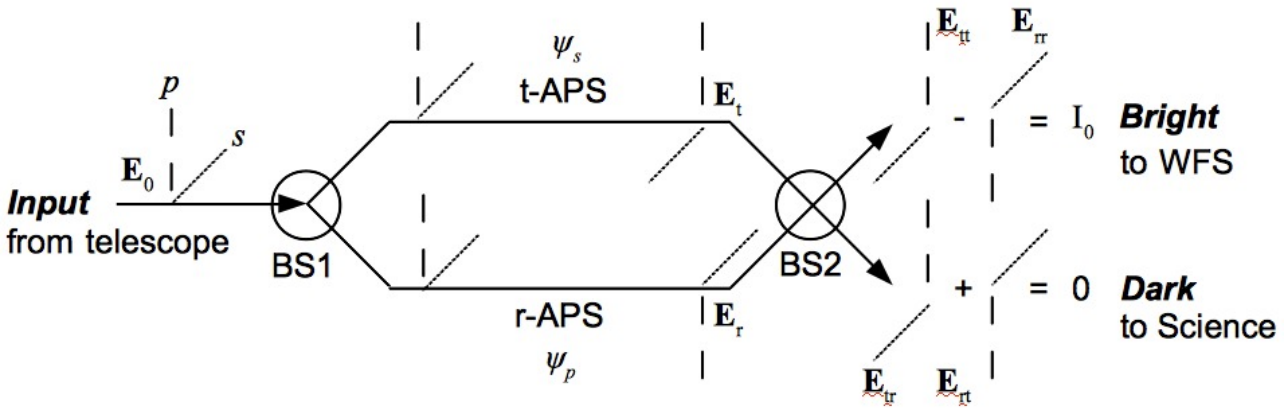

Figure 1. The principle of operation of polarization-based interferometric nulling. The dashed and dotted lines representing the respective p- and s-polarization components common to the beamsplitter (BS1) and beam combiner (BS2) are retarded independently by $\psi = \pi$ in each arm. The subscripts t and r denote beamsplitter reflection and transmission, respectively. Beamsplitter and common phase factors introduced by fold mirrors, path, and the Fresnel rhombs are not indicated in the orientation of the polarization components to emphasize the effect of the rhombs.

2. BROADBAND VISIBLE NULLING CORONAGRAPH DEMONSTRATION

One of the main challenges facing direct detection of exoplanetary system light is broadband suppression of scattered starlight for increased sensitivity and spectroscopic observations. For a nulling interferometer, this requires introducing a phase shift between interfering arms as near to π as possible over the required bandpass. The effect by which the VNC will accomplish this is through retardance, a difference in phase shift between polarization components by an optical element or interface. A schematic of such a system is shown in Fig. 1.

Treating the retarder as an arbitrary pair of elements, one in each arm of an interferometer, the system is fed with an input field

$$\mathbf{E}_0 = E_0 \begin{pmatrix} \cos\theta \\ \sin\theta \end{pmatrix}, \tag{1}$$

where θ is the polarization angle and omitting common phase factors due to path and fold mirrors. Following traversal of the first beamsplitter and retarders, the fields in each arm may be written as

$$\mathbf{E}_t = E_0 \begin{pmatrix} t_\perp e^{i\psi} \cos\theta \\ t_\parallel \sin\theta \end{pmatrix} \quad \mathbf{E}_r = E_0 \begin{pmatrix} r_\perp e^{i\xi_\perp} \cos\theta \\ r_\parallel e^{i(\psi+\xi_\parallel)} \sin\theta \end{pmatrix} \tag{2}$$

where ξ is the difference in phase between the reflected and transmitted beams.

In the bright, asymmetric output the fields may be written as

$$\mathbf{E}_{tt} = E_0 \begin{pmatrix} t_\perp^2 e^{i\psi} \cos\theta \\ t_\parallel^2 \sin\theta \end{pmatrix} \quad \mathbf{E}_{rr} = E_0 \begin{pmatrix} r_\perp^2 e^{i2\xi_\perp} \cos\theta \\ r_\parallel^2 e^{i(\psi+2\xi_\parallel)} \sin\theta \end{pmatrix} \tag{3}$$

where $\psi = \phi_s - \phi_p$ is the *local* phase retardance, r and t denote reflected or reflectance and transmitted or transmittance. In the dark, symmetric output the fields may be written as

$$\mathbf{E}_{tr} = E_0 \begin{pmatrix} t_\perp r_\perp e^{i(\psi+\xi_\perp)} \cos\theta \\ t_\parallel r_\parallel e^{i\xi_\parallel} \sin\theta \end{pmatrix} \quad \mathbf{E}_{rt} = E_0 \begin{pmatrix} r_\perp t_\perp e^{i\xi_\perp} \cos\theta \\ r_\parallel t_\parallel e^{i(\psi+\xi_\parallel)} \sin\theta \end{pmatrix} \tag{4}$$

For the ideal $\psi = \pi$ retarder used with a lossless, polarization independent 50/50 beamsplitter ($\xi = \pi/2$), the dark and bright output intensities are

$$I_b = |\mathbf{E}_{tt} + \mathbf{E}_{rr}|^2 = \frac{I_0}{2}(1 - \cos\psi) = I_0 \tag{5}$$

$$I_d = |\mathbf{E}_{tr} + \mathbf{E}_{rt}|^2 = \frac{I_0}{2}(1 + \cos\psi) = 0 \tag{6}$$

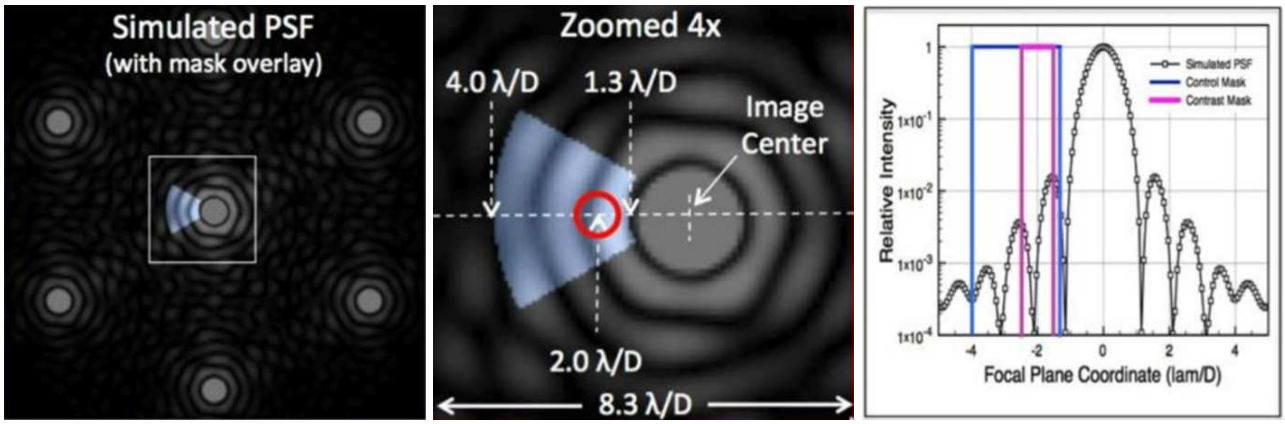

Figure 2. *Dark hole region, location, and size.* Left – 512×512 dark hole region overlay on simulated PSF. Center – control modes are designed to achieve 10^{-9} contrast over 40 nm bandpass within the wedged region ($4\times$ scale of left panel) with the circle of diameter $1\lambda/D$ centered at $2\lambda/D$ showing the region over which the contrast is calculated. Right – plot from left to right along the dashed line in the central panel showing the control mask extending from -4 to $-1.3\lambda/D$.

Real beamsplitters and retarders influence the complex wavefront in a chromatic and polarization dependent manner. Material dispersion and absorption introduce gradients in transmission, reflection, and phase coefficients. Material and fabrication defects introduce spatial non-uniformities not limited to geometric and polishing errors, inclusions and striae, residual and mechanical stress induced birefringence, as well as coating layer thickness variation and contamination. In order to meet the stringent phase, amplitude, and polarization symmetry requirements for 10^{-9} contrast, tolerances on these as well as ambient environmental properties including thermal and mechanical dynamics must be considered. Here we present the design of the APS within the overall system tolerances and wavefront sensing and control (WFS/C) capability of the VNC.

One approach to the tolerancing effort is to determine the necessary pupil plane contrast required to meet a given contrast in the image plane dark hole (see Fig. 2). Determination of this factor allows for tolerancing and specification of the APS without having to perform a computationally intensive full propagation to the image plane including simulated WFS/C. The first factor to consider is diffraction attributed to the aperture function. For a roughly circular shape the polychromatic point spread function (PSF) may be approximated with the asymptotic form

$$\mathrm{PSF}(\mu) \sim \left[1 + \frac{\pi^4}{8}|\mu|^3\right]^{-1} \tag{7}$$

where μ is the field angle in units of λ/D. Performing an expansion of Eq. 6 that is modified to include phase, amplitude, and polarization asymmetries, the contrast in the image plane may be approximated as

$$C(\mu) \sim \frac{\sigma_{DH}^2/\sigma_T^2}{1 + \frac{\pi^4}{8}|\mu|^3}\left(\frac{\sigma_\phi^2}{4} + \frac{\sigma_I^2}{16} + \frac{\sigma_\psi^2}{4}\right) \tag{8}$$

where σ_{DH}^2 is the wavefront variance contained within the spatial frequencies corresponding to the image plane dark hole and σ_T^2 is the total wavefront variance at all spatial frequencies given by the 2D integral of the PSD over all spatial frequencies. The terms $\{\sigma_\phi^2, \sigma_I^2, \sigma_\psi^2\}$ are the total variances, i.e. at all spatial frequencies, for phase errors, intensity errors, and polarization errors, respectively. Calculating the fractional power of these errors within the spatial frequency range of interest enables specification of the suppression that needs to be achieved in the pupil, and the total RMS surface figure error, coating uniformity, and polarization variation.

The VNC uses a hexagonally-packed segmented deformable mirror, the multiple mirror array (MMA),[11] for phase control across the instrument beam attributed to coating and polishing defects introduced by each element in the optical train. The approach to WFS/C is described in more detail in Sec. 2.2. Here it suffices to state that wavefront control is performed in such a way to balance phase, amplitude, and polarization effects to optimize

contrast within a range of spatial frequencies corresponding to the dark hole region of the science image plane. Determining exactly how much wavefront error power propogates to the dark hole would require knowledge of the input field and the complex transmission properties of each surface and their relative positions. When these exact characteristics are not known, as is necessarily the case for optics that have not yet been fabricated, typical surface figure and coating non-uniformity profiles take a two-dimensional power spectral density (PSD) of the form

$$\mathrm{PSD}(f) = \frac{\alpha}{2\pi^2 f_k^2} \sin\left(\frac{2\pi}{\alpha}\right) \frac{\sigma_T^2}{1+(f/f_k)^\alpha} \quad \text{for } \alpha > 2, \tag{9}$$

where $f = \sqrt{f_x^2 + f_y^2}$ and f_k are the radial spatial frequency and knee frequency, respectively, and both are in units of cycles per aperture (cpa), or equivalently units of λ/D in sky angle, and the exponent in the power law is typically on the order of 2 to 3. The broadband demonstration of the VNC will target the same wedge-shaped dark hole as the narrowband demonstration spanning $1.3 - 4\lambda/D$ in radius and 60°in azimuth, with the outer working angle (OWA) of the dark hole being limited by the number of rings in the hexagonal array. Of particular interest for meeting the next VNC Technology Demonstration for Exoplanet Missions (TDEM) broadband milestone is the root-mean-square (RMS) and peak-to-valley (PV) wavefront error in the critical spatial frequency band extending from $1.5 - 2.5$ cpa and over an angle of 60°, for which the fractional power may be calculated from the integral:

$$\sigma^2_{f_L \to f_H} = \frac{\alpha \sigma_T^2}{2\pi^2 f_k^2} \sin\left(\frac{2\pi}{\alpha}\right) \int_{-\pi/6}^{\pi/6} \int_{f_L}^{f_H} \frac{1}{1+(f/f_k)^\alpha} f \, \mathrm{d}f \, \mathrm{d}\phi \tag{10}$$

Assuming a value of 3 for α, this may be evaluated to:

$$\sigma^2_{f_L \to f_H} = \frac{\sigma_T^2 \sqrt{3}}{24\pi} \left\{ 2\sqrt{3} \left[\tan^{-1}\left(\frac{f_k - 2f_L}{\sqrt{3} f_k}\right) - \tan^{-1}\left(\frac{f_k - 2f_H}{\sqrt{3} f_k}\right) \right] + 2\ln\left(\frac{f_L + f_k}{f_H + f_k}\right) + \ln\left(\frac{f_H^2 - f_H f_k + f_k^2}{f_L^2 - f_L f_k + f_k^2}\right) \right\} \tag{11}$$

Making the final assumption that $f_k = 1$, this gives for the bands

$$\begin{aligned}
\sigma^2_{0\to\infty} &= 0.166667\sigma_T^2 \Rightarrow \sigma_{0\to\infty} = 0.408248\sigma_T \\
\sigma^2_{0\to1.5} &= 0.0806277\sigma_T^2 \Rightarrow \sigma_{0\to1.5} = 0.283950\sigma_T \\
\sigma^2_{1.5\to2.5} &= 0.0317574\sigma_T^2 \Rightarrow \sigma_{1.5\to2.5} = 0.178206\sigma_T \\
\sigma^2_{2.5\to\infty} &= 0.0542816\sigma_T^2 \Rightarrow \sigma_{2.5\to\infty} = 0.232984\sigma_T
\end{aligned}$$

where the top row is the integral of all spatial frequencies but only in a 60° arc and where the following three rows represent the three spatial frequency bands. Note that $\sigma^2_{0\to\infty} = \sigma^2_{0\to\infty} + \sigma^2_{0\to\infty} + \sigma^2_{0\to\infty} = 0.166667\sigma_T^2$. Thus the sum of the power in the 3 bands gives 1/6 of the total power since we integrate over 60° or 1/6 of 360°. Approximately 3% of the wavefront power (17.8% of the RMS error) is contained in the TDEM critical $1.5 - 2.5$ cpa band. Taking this result over the critical spatial frequency band centered at 2 cpa spatial frequency Eq. 8 may be rewritten as:

$$C\left(2\frac{\lambda}{D}\right) = 3.2271 \times 10^{-4} \left(\frac{\sigma_\phi^2}{4} + \frac{\sigma_I^2}{16} + \frac{\sigma_\psi^2}{4}\right) \tag{12}$$

Finally, the RMS result may be scaled to PV variation by multiplying by $2\sqrt{2} = 2.828$, the value of which may not exceed the MMA stroke reserved for wavefront correction. With these relations determined, an overall error budget for the VNC can be set, and the VNC APS may be designed and specified.

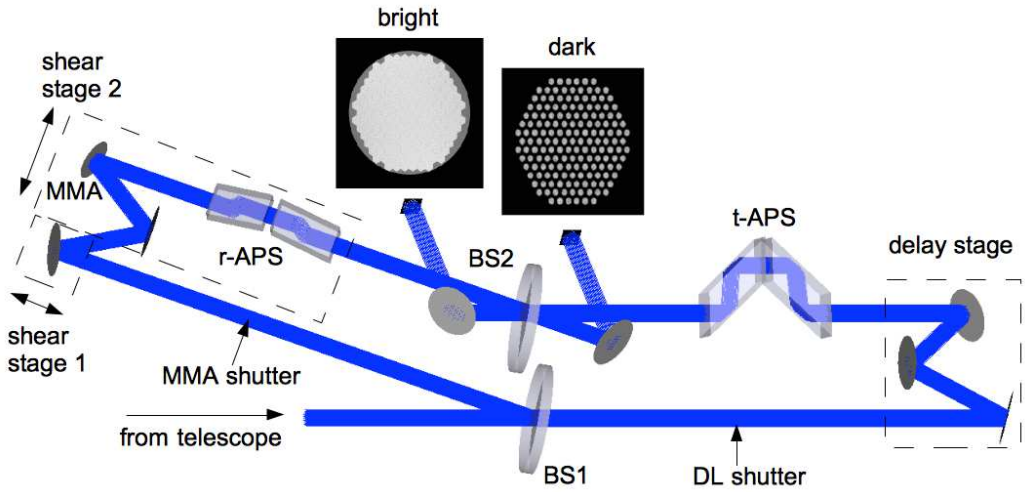

Figure 3. The VNC model for performing sensitivity and compensation analysis used to tolerance the Fresnel rhombs APS that will be fabricated and integrated with the VNC to demonstrate 10^{-9} contrast over a 40 nm bandwidth centered at 633 nm. The APS consists of two pairs of symmetric Fresnel rhombs that are coated on the TIR surfaces to produce a broadband $\pi/4$ retardance at each reflection. The pairs are oriented orthogonally to one another in terms of their respective s- and p-plane reflections.

2.1 Fresnel Rhomb Achromatic Phase Shifters

Crossed Fresnel rhomb pairs provide a means by which a π phase delay can be introduced between interferometer arms and this is the method being pursued for the broadband VNC demonstration. The planned layout for inclusion within the VNC is shown in Fig. 3. By choosing an appropriate prism material of index $n_g(\lambda)$ and TIR angle of incidence (AOI), γ, a narrow band $\pi/4$ retardance for each reflection can be found to satisfy

$$\Delta\Phi_{s-p}(\lambda) = 2\tan^{-1}\left[\frac{\sqrt{\sin^2\gamma - n^2(\lambda)}}{n^2(\lambda)\cos\gamma}\right] - 2\tan^{-1}\left[\frac{\sqrt{\sin^2\gamma - n^2(\lambda)}}{\cos\gamma}\right] \tag{13}$$

where $n(\lambda) = n_a(\lambda)/n_g(\lambda)$ is the ratio of the ambient index of refraction, $n_a(\lambda)$, to that of the glass.

Lithosil fused silica has been chosen for the fabrication of the Fresnel rhombs based on its homogeniety and low levels of striae, bubbles, and inclusions. The peak retardance for a single internal reflection (with equal to or near unity ambient index) occurs at $\gamma = 53°$ and is only 0.74 rad at 633 nm. Thin-film coatings can be applied

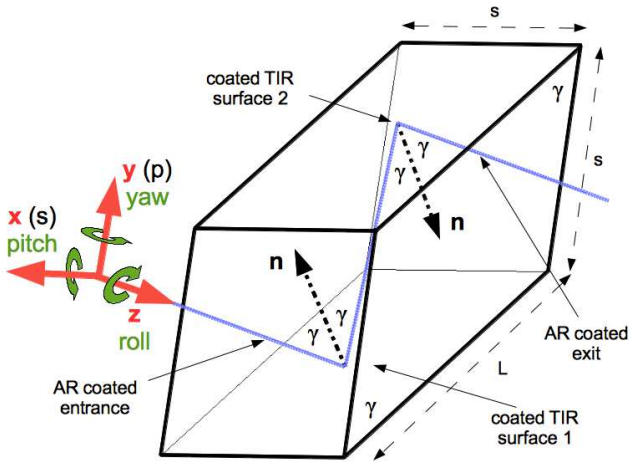

Figure 4. VNC APS single Fresnel rhomb schematic. The entrance and exit surfaces are AR coated to $< 0.1\%$ and the TIR surfaces are modeled as being coated with the prescription that ideally produces the broadband retardance shown in Fig. 5 (following four reflections, two in each prism). The rhombs' acute angles are equal to the TIR angle of incidence, γ. Light enters each Fresnel rhomb at normal incidence propagating along the local z/roll-axis. The TIR p-polarization component lies in the y-z plane. Pitch and yaw are defined as rotation about the local x- and y-axis, respectively, and are clocked at 90°between interferometer arms. The local axes are shown offset in negative z from the model center of rotation, which is located at the center of the entrance face.The location of each axis of rotation for each rhomb is yet to be defined in the actual VNC breadboard.

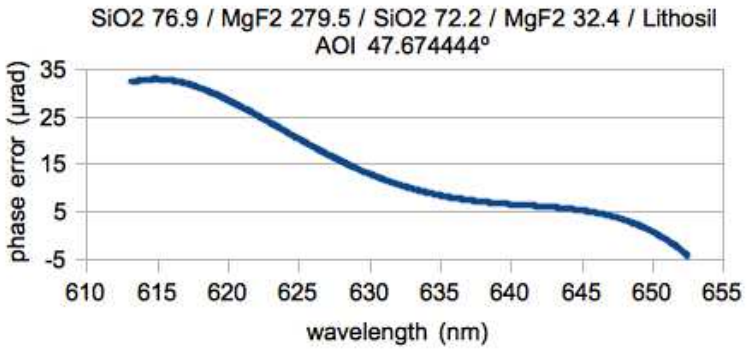

Figure 5. The difference from π retardance for the coated TIR solution presented in this work. Bulk dispersion properties were assumed for each material in order to generate a coating solution for the geometric and positional sensitivity study. The rms phase error for this design is 18 µrad over the 40 nm target bandpass. In practice, layer thickness- and material interface-dependent dispersion properties must be used to refine a solution that meets performance requirements that can be modeled to predict coating thickness, rhomb geometry, and rhomb alignment sensitivities.

to each of the eight TIR surfaces for added phase shift between polarization components, and can be tuned to realize a broadband π retardance within the allotted 3×10^{-4} rad rms in the overall VNC error budget. The approach to finding such a coating solution is presented in a previous work.[8] Of the several solutions generated, a 4-layer coating consisting of alternating layers of silicon dioxide and magnesium flouride was selected based on its favorable performance over the 613-653 nm broadband VNC bandpass. The plot of $\Delta\Phi_{s-p}(\lambda) - \pi$ for this solution is shown in Fig. 5, which has a phase error of 18 µrad RMS. The solution finder and corresponding modeled performance assumes bulk dispersion properties for each material. The actual coating prescription will be refined based on experience characterizing dispersion effects introduced by deposition processes and inter-layer strain.

Geometric tolerancing of the rhombs flows from the coating design and requirement that 99% of the diffraction envelope be contained within the clear aperture. For the coating solution in this work, $\gamma = 47.67444°$, which yields a longest edge dimension of $L = 24.4$ mm and projected length of 18.0 mm along the undeviated beam. The entrance and exit faces are over-sized to accommodate Fresnel ringing. Given their location relative to the MMA pupil plane, the rhombs are sized to $s = 15.0$ mm on edge at the entrance and exit faces in order to accommodate up to a 10.8 mm pupil and allow for clear aperture margin.

Having determined these basic parameters, a tolerancing study was performed to set the rhomb specifications for fabrication. This was done by first evaluating the *uncompensated* sensitivity of individual rhomb facet errors using the model shown in Fig. 3, which calculates pupil suppression (leakage) as the sum of the ratio of dark to bright output coherent intensities at each polarization. The polynomial fits to each prism's measured sensitivity to asymmetries in size and parallelism of the entrance and exit surfaces and coated TIR surfaces is shown in Fig. 6. The fabrication error that is most tolerable is the deviation of the entrance and exit surface plane normals relative to the rest of the optic, which introduces refraction according to Snell's law that gives rise to pupil

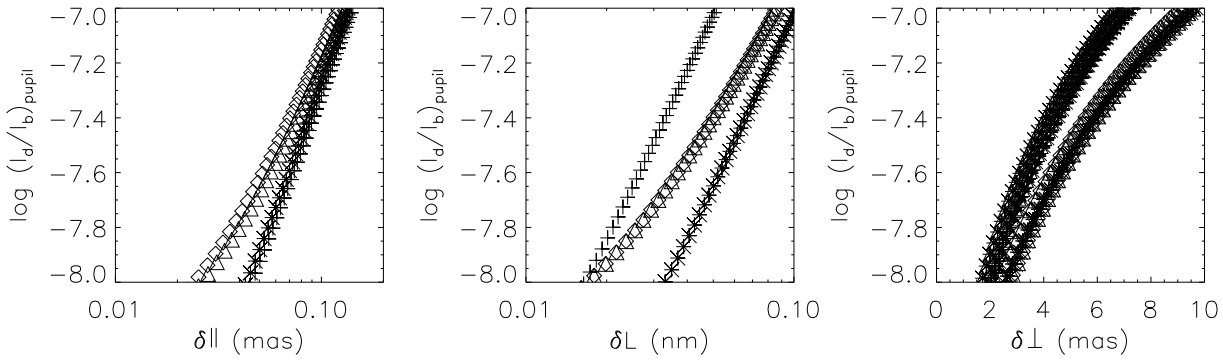

Figure 6. Pupil plane leakage sensitivity to variation in each rhomb's geometry including TIR surface parallelism (left), long edge length (center), and tilted surface errors in two directions for the entrance and exit of each prism for a total of 16 sensitivity curves (right). Each symbol corresponds to one of the four rhombs.

location dependent and chromatic path variation as well as polarization dependent transmission and refraction coefficients. Pure dimensional errors introduce dispersion at 0 cpa spatial frequency and are compensated by adjusting the path delay according to Fig. 3. Deviation from parallelism between the TIR surfaces compromises the broadband retardance coating solution and implies refraction at one or both of the entrance surfaces if they are parallel.

Without compensation, the prisms would need to be fabricated roughly to the precision of each abscissa's maximum in order to meet the $\sim 10^{-7}$ pupil plane leakage requirement for the APS inside the overall system budget. For instance, if all angles are fabricated perfectly and the rhombs are perfectly aligned, but the length of a rhomb is off by 1 Å in one dimension relative to the others, then the difference in dispersion between air and Lithosil over this difference across the 40 nm bandpass is the limit to what can be tolerated for the system to still meet performance requirements. For all practical purposes, without compensation a tens of *microarcsecond* parallelism requirement would render this approach unfeasible. The ability to compensate for these errors through rotational positioning of the rhombs using active tip, tilt, and rotation mechanisms as well as a delay line relaxes the requirements on the fabricated prism angles.

2.2 Broadband Wavefront Sensing and Control

There are two main control components of the VNC WFS/C: (1) low spatial frequency correction that introduces a polychromatic π phase shift between interfering arms via positioning of the Fresnel rhombs APS in tip, tilt, and roll, and (2) high spatial frequency correction from a deformable mirror, the MMA, located at a pupil in one arm of the nuller cavity. The layout of these components is shown in Fig. 3. The APS comprise a new addition to the VNC that is currently in the procurement stage of development. A sketch of the planned approach to positioning the APS precedes a description of the more mature method used to perform dark hole optimization with the MMA that is presented in the VNC TDEM Milestone #1 Report.[12]

The positional sensitivity of the rhombs was determined using a method similar to that which was used for the geometrical sensitivity as described in Sec. 2.1. Model parameters for the layout shown in Fig. 3 consistent with the existing VNC and coating prescription given in Fig. 5 were perturbed to the point where the tolerable pupil contrast was reached. Polynomial fits to positional sensitivities are plotted in Fig. 7 for each rotational degree of freedom, pitch, yaw, and roll, as shown in Fig. 4 for each of the four rhombs. In each of these plots, the rhombs are geometrically perfect and only a single misalignment is introduced of the $N_{DOF,APS} = 3 \times N_{rhombs} = 12$ relative to the instrument coordinate system. Sensitivities are determined following each update to the set of rhomb positions.

Positional control of the rhombs will be achieved through what is presently envisioned as a tiered system of a tip/tilt PZT giving pitch and yaw control mounted on a rotational mount similar to what is used for linear

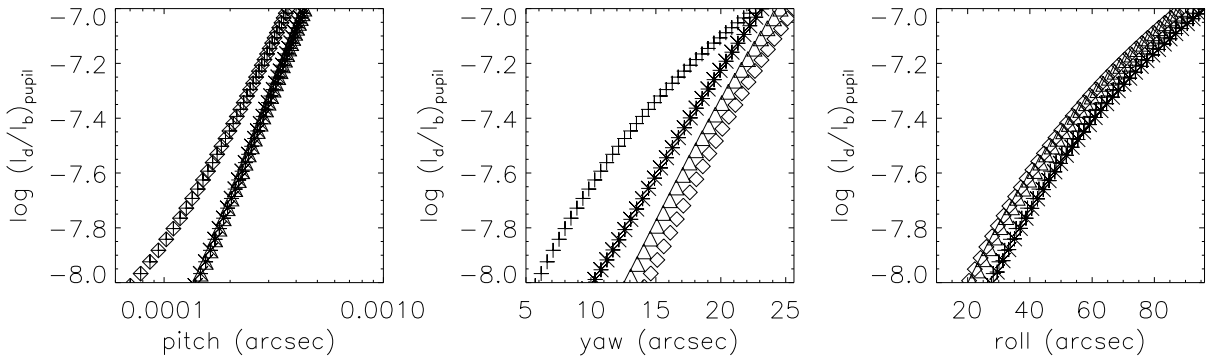

Figure 7. Pupil plane leakage sensitivity to each rhomb's pitch (left), yaw (center), and roll (right). Each of these degrees of freedom is controlled to compensate for leakage attributed to geometrical asymmetries shown in Fig. 6. What appears to be an alarming pitch positional requirement of 0.5 mas (2.4 nrad) that is $\sim 1/20 - 1/40$ the resolution of current PZT tip-tilt stage, actually manifests itself predominantly as a piston error with a small amount of chromatic shear, the former of which is accommodated with a delay line.

polarizers for roll. The rhombs will ultimately either (1) be individually mounted, with a maximum of one mounted in a fixed position relative to the VNC, set to ~ 1 arcsec accuracy in pitch and yaw, and better than 1 armin in roll, or (2) mounted as pairs that have either been aligned and affixed to a common interface or optically contacted. The first option offers a greater number of active control degrees of freedom at the cost of high complexity and instability, while the second option simplifies the routine operation rhomb alignment effort and can increase stability assuming the pairs can be joined with adequate precision.

For higher order spatial frequency wavefront control, the VNC uses the MMA to first suppress the pupil, then optimize contrast within the dark hole shown in Fig. 2. Controlling each of the MMA's hexagonal segments in piston, tip and tilt by 3 voltage driven actuators in closed-loop allows the VNC to increase the contrast within the dark hole. Iterative closed-loop control allows deeper contrast to be obtained and held. Each actuator voltage is controlled in software. Each of the MMA segments' piston, tip, and tilt influence functions are orthogonal in that motion of one doesn't influence the wavefront of the others. However, since we desire a dark hole in a specific focal plane region it is more efficient to couple linear combinations of actuators together into a set of control modes. This results in a smaller set of control modes enabling a trade between higher control bandwidth and instrument level temporal stability. The set depends on the size and location of the dark hole region and on the sensing noise floor due to vibration and camera noise. The procedure used for the design of the set of control modes is discussed in the following.

First, a set of orthogonal basis column vectors, $\mathbf{B}_j$ is generated. Each basis vector represents either piston, tip, or tilt in the pupil (plane of the MMA), where the number of basis vectors is equal to the number of degrees of freedom, $N_{DOF,MMA} = 3 \times N_{seg} = 474$, where $N_{seg} = 158$ is the total number of valid segments; thus $j = 1, ..., N_{DOF,MMA}$. Each basis vector is a column vector consisting of a 2D pupil image of size $N_S = 512 \times 512$ discrete samples lexigraphically reordered into a 1D column vector of length 512^2.[13] Each basis vector represents pure piston, tip or tilt of a single MMA segment and each is normalized such that it is orthonormal in the sense that $\mathbf{B}_j \cdot \mathbf{B}_k = \{1 \text{ for } k = j, 0 \text{ for } k \neq j\}$. The set of basis vectors are combined column-wise to construct the influence matrix $\mathbf{R} = [\mathbf{B}_1, \mathbf{B}_2, ..., \mathbf{B}_{N_{DOF,MMA}}]$ where each influence matrix column vector is the j-th basis vector, and where each basis vector is mapped to the voltage of a single MMA segment's controllable DOF. Since the influence vectors (columns) are orthonormal, the matrix $\mathbf{R}^T\mathbf{R}$ is diagonal of size 474×474, with zero off-diagonal elements and unity diagonal elements. Linear combinations of these basis vectors span all command motions of the MMA. This basis, however, is not optimal within the region of the dark hole.

The dark hole region is incorporated by numerically propagating each basis vector through the simulated VNC via the small angle approximated equation given by $\tilde{\mathbf{P}}_j = -\frac{i}{2}k\mathbf{H}\mathbf{B}_j$ where $\mathbf{H}$ is the discrete Fourier transform operator such that its output has the same plate scale (sampling) as the lab VNC. The dark hole region is imposed by averaging the dot products of the focal plane complex fields over the region of the dark hole

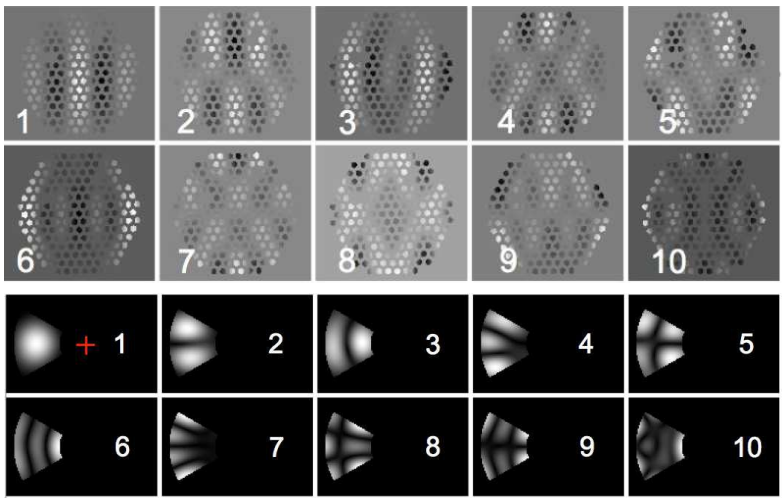

Figure 8. The first ten of 200 MMA control modes of greatest influence for optimizing the VNC dark hole.

Figure 9. The corresponding first ten of 200 focal plane intensity patterns.

resulting in a complex self-adjoint matrix for the jk basis vectors given by:

$$[\mathbf{J}]_{jk} = \frac{1}{N_H} \sum_{m=1}^{N_H} M_m [\tilde{\mathbf{P}}_j^{\dagger} \cdot \tilde{\mathbf{P}}_k]_m \tag{14}$$

The mask representing the dark hole is given by M_m for $m \in [1, N_H]$ where N_H is the total number of samples within the dark hole, and since the focal plane fields are sampled at the VNC sampling it implicitly incorporates the sampling as part of the design procedure. The mask is unity within the dark hole and zero outside it.

The matrix $\mathbf{J}$ is given by the conjugate dot product of the mask weighted focal plane fields averaged over the region of mask and $\mathbf{J}$ is an $N_{DOF,MMA} \times N_{DOF,MMA}$ square complex self-adjoint (equal to its transpose conjugate) with real eigenvalues. The diagonal elements are real since they are the modulus squared, but $\mathbf{J}$ is not in general diagonal. The non-zero off-diagonal elements imply that the basis vectors have crosstalk. The crosstalk is eliminated by diagonalizing $\mathbf{J}$ using singular value decomposition (SVD) to find the unitary transformation such that $\mathbf{U}^{\dagger}\mathbf{J}\mathbf{U}$ is diagonal. The resultant SVD eigenvalues are then reordered such that the first basis vector (eigenvector) gives the largest change within the region of the dark hole with successive basis vectors giving progressively smaller changes.

Each of the diagonal focal plane fields are separately back-propagated to the pupil plane of the MMA via inverse Fourier transforms and are renormalized such that the modulus squared over the region of the valid segments is unity. This new set of basis vectors are orthonormal and form a unique set of linear combinations of segment piston, tip, and tilt (Fig. 8) that gives the largest change per mode over the region of the dark hole (Fig. 9). It is expected that this already demonstrated control of the MMA combined with the control of the Fresnel rhomb APS using active positioners and a delay line will enable the broadband demonstration of the VNC at 10^{-9} contrast at $2\lambda/D$.

3. FUTURE WORK: SEGMENTED APERTURE DEMONSTRATION

In order to demonstrate operation of the VNC with a segmented primary mirror input, we plan to replace the circular segments of the Fizeau Interferometry Testbed (FIT)[14] (see Fig. 10), with actuated and movable hexagonal segments. This enhanced-fidelity testbed, known as the Segmented Aperture Interferometric Nulling Testbed (SAINT), will conduct the first demonstration of segmented-aperture coronagraphy. SAINT is a laboratory testbed for developing segmented aperture high-contrast imaging, and a successful demonstration of the system

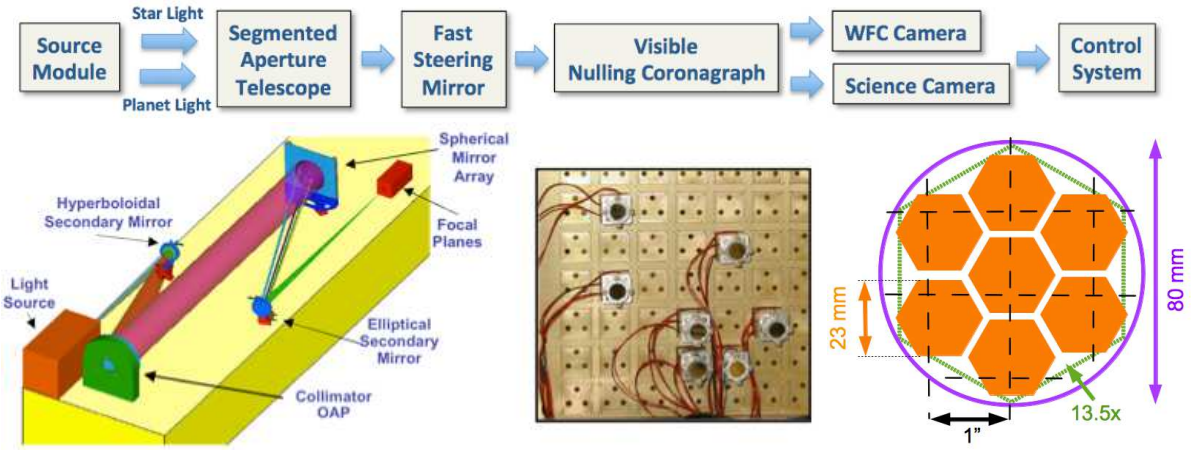

Figure 10. Block diagram (top), existing FIT layout schematic (bottom left), FIT spherical mirror array with 12 mm circular sub-apertures on a 1" grid (bottom center), and the overlay of 23 mm hexagonal sub-apertures mounted on the FIT 1" grid backplane and VNC tip/tilt/piston deformable mirror at 13.5X magnification. The sub-apertures could be generated by dicing an 80 mm diameter parent mirror that is polished to $\lambda/20$. A minimum of three sub-apertures will be used in the demonstration.

will significantly impact the design of ATLAST by providing the opportunity to develop WFS/C algorithms for the VNC optimized for segmented mirrors.

Components of SAINT are depicted in Fig. 10, including the existing FIT framework and new innovative element: a set of hexagonal mirrors cleaved from a single parent polished with a concave spherical surface positioned relative to one another in order to form a coherent aperture. SAINT will consist of a minimum of three independently actuated mirrors (see Fig. 10), to achieve $\leq 10^{-8}$ contrast with the VNC, initially performed over the 40 nm bandpass targetet in Sec. 2. This segmented aperture will be aligned with the existing FIT optics to form a telescope for demonstrating one of the key features of the VNC: high-contrast functionality with arbitrary apertures. It will have a wavelength range that is comparable to ATLAST, including high sensitivity from 0.1 to 2.4 µm and diffraction limited imaging at 0.5 µm

In conclusion, in addition to operating broadband with an arbitrary segmented aperture, environmental and control stability issues that must be tolerated by a flight system will be present and controllable in SAINT, enabling the opportunity to study a range of issues that will need to be addressed on the development path pushing to higher contrast limits at higher resolution for of the next great observatory.

ACKNOWLEDGMENTS

BAH is a Fellow of the NASA Postdoctoral Program administered by Oak Ridge Associated Universities.

REFERENCES

[1] Clampin, M., Melnick, G., Lyon, R., Kenyon, S., Sasselov, D., Tolls, V., Ford, H., Golimowski, D., Petro, L., Hartig, G., Sparks, W., Illingworth, G., Lin, D., Seager, S., Weinberger, A., Harwit, M., Marley, M., Schneider, J., Shao, M., Levine, M., Ge, J., and Woodruff, R., "Extrasolar planetary imaging coronagraph (EPIC)," *Proc. SPIE* **6265** (July 2006).

[2] Lyon, R. G., Clampin, M., Woodruff, R. A., Vasudevan, G., Ford, H., Petro, L., Herman, J., Rinehart, S., Carpenter, K., and Marzouk, J., "Balloon exoplanet nulling interferometer (BENI)," *Proc. SPIE* **7440** (Aug. 2009).

[3] Lyon, R. G., Clampin, M., Petrone, P., Mallik, U., Madison, T., and Bolcar, M. R., "High contrast vacuum nuller testbed (VNT) contrast, performance, and null control," *Proc. SPIE* **8442** (Sept. 2012).

[4] Content, D. A., Armani, N. V., Baker, C. L., Jackson, C. E., Kahle, D. M., Kruk, J. W., Lehan, J. P., Melton, M. E., Mentzell, E., Miko, J. J., Palace, D. J., Pasquale, B. A., Peabody, H. L., Smith, B. S., Smith, W. F., Stewart, J. W., Vaughnn, D. A., Waczynski, A., and Wallace, T. E., "Wide field instrument preliminary design for the Wide Field InfraRed Survey Telescope," *Proc. SPIE* **8860** (Sept. 2013).

[5] Postman, M., Brown, T., Sembach, K., Giavalisco, M., Traub, W., Stapelfeldt, K., Calzetti, D., Oegerle, W., Michael Rich, R., Phillip Stahl, H., Tumlinson, J., Mountain, M., Soummer, R., and Hyde, T., "Advanced Technology Large-Aperture Space Telescope: science drivers and technology developments," *Optical Engineering* **51**, 011007 (Jan. 2012).

[6] Morgan, R. M., Burge, J. H., and Woolf, N. J., "Final laboratory results of visible nulling with dielectric plates," *Proc. SPIE* **4838**, 644–655 (Feb. 2003).

[7] Mawet, D., Hanot, C., Lenaers, C., Riaud, P., Defrère, D., Vandormael, D., Loicq, J., Fleury, K., Plesseria, J. Y., Surdej, J., and Habraken, S., "Fresnel rhombs as achromatic phase shifters for infrared nulling interferometry," *Optics Express* **15**, 12850 (Sept. 2007).

[8] Bolcar, M. R. and Lyon, R. G., "Approaches for achieving broadband achromatic phase shifts for visible nulling coronagraphy," *Proc. SPIE* **8445** (July 2012).

[9] Baudoz, P., Rabbia, Y., and Gay, J., "Achromatic interfero coronagraphy I. Theoretical capabilities for ground-based observations," *Aston. Astrophys. Sup.* **141**, 319–329 (Jan. 2000).

[10] Ren, D. and Serabyn, E., "Symmetric nulling coronagraph based on a rotational shearing interferometer," *Appl. Opt.* **44**, 7070–7073 (Nov. 2005).

[11] Helmbrecht, M. A., He, M., and Kempf, C. J., "High-actuator-count MEMS deformable mirrors," *Proc. SPIE* **8725** (May 2013).

[12] Clampin, M., Lyon, R., Petrone III, P., Mallick, U., Bolcar, M., Madison, T., and Helmbrecht, M., "Visible nulling coronagraph technology maturation: High contrast imaging and characterization of exoplanets," tech. rep., NASA Goddard Space Flight Center (2013).

[13] Murphy, T. P., Lyon, R. G., Dorband, J. E., and Hollis, J. M., "Sparse matrix approximation method for an active optical control system," *Appl. Opt.* **40**, 6505–6514 (Dec. 2001).

[14] Lyon, R. G., Carpenter, K. G., Mazzuca, L., Huet, H., Cottle, P. W., Petrone, III, P. P., Dagoda, P., Liiva, P., Marzouk, J., Solyar, G., Mozurkewich, D., Zhang, X., and Armstrong, T., "Fizeau interferometry testbed: wavefront control," *Proc. SPIE* **5487**, 963–974 (Oct. 2004).